Available online at www.sciencedirect.com
SCIENCE DIRECT®
Journal of Magnetic Resonance 174 (2005) 270–278
JMR Journal of Magnetic Resonance
www.elsevier.com/locate/jmr

Triple-quantum-filtered imaging of sodium in presence of B_0 inhomogeneities

Costin Tanase [a,b,*], Fernando E. Boada [b]

[a] Department of Physics and Astronomy, University of Pittsburgh, 35905 O'Hara Street, Pittsburgh, PA 15213, USA
[b] MR Research Center, University of Pittsburgh Medical Center, 200 Lothrop Street, Pittsburgh, PA 15213, USA

Received 21 November 2004; revised 8 February 2005
Available online 14 March 2005

Abstract

Triple quantum filtered sodium MRI techniques have been recently demonstrated in vivo. These techniques have been previously advocated as a means to separate the sodium NMR signal from different physiological compartments based on the differences between their relaxation rates. Among the different triple quantum coherence transfer filters, the three-pulse coherence transfer filter has been demonstrated to be better suited for human imaging than the traditional four-pulse implementation. While the three-pulse structure has distinct advantages in terms of RF efficiency, the lack of a refocusing pulse in the filter introduces an increased dependence on the main magnetic field inhomogeneities, which can sometimes lead to significant signal loss. In this paper, we characterize these dependencies and introduce a method for their compensation through the acquisition of a B_0 map and the use of a modified phase cycling scheme.
© 2005 Elsevier Inc. All rights reserved.

Keywords: Multiple quantum filter; Imaging; Coherence; Inhomogeneity

1. Introduction

Multiple quantum filtered (MQF) techniques have been used extensively in NMR to separate the NMR signal from environments where non-negligible, second-order, contributions to the Zeeman Hamiltonian allow for non-trivial nuclear transitions. In the case of sodium, a very important ion in cell physiology, these techniques have been further explored for the separation of the NMR signal between the intra- and extra-cellular compartments in the context of animal models of disease [1]. Triple quantum sodium NMR techniques, in particular, have been used for the observation of sodium ion shifts during ischemia [2] and for the identification of neoplastic changes in human and/or animal tissues [1,3]. While well known in the NMR literature, the conventional implementation of TQ sodium NMR relies on the use of a four RF pulse coherence transfer filter. In this four pulse structure, the first pulse creates coherences that evolve freely and are refocused by the second RF pulse before being converted into triple quantum coherences and observable magnetization by the third and four pulses, respectively. As shown by Hancu et al. [4], the four pulse structure, while being well suited for NMR experiments over small samples, introduces a strong dependence on the RF field leading to strong, and difficult to compensate, signal modulation across the field of view when imaging applications are considered. By eliminating the second RF pulse from this structure, the signal dependence on the RF field becomes less severe [4,5] and, moreover, this dependence factors out from that of all other experimental parameters. This feature of the three-pulse coherence transfer filter makes it better suited for imaging experiments because the aforementioned factorization allows for compensation of the

* Corresponding author. Fax: +1 4126479800.
E-mail address: tanc@phyast.pitt.edu (C. Tanase).

1090-7807/$ - see front matter © 2005 Elsevier Inc. All rights reserved.
doi:10.1016/j.jmr.2005.02.012

signal modulation using an estimate of the B_1 field across the field of view [4,5].

The three-pulse implementation of TQ sodium MRI has been demonstrated on human subjects and has been used for the observation of neoplastic changes in the human brain. This implementation, because of the lack of a refocusing pulse during the preparation period, introduces a signal dependence on the main magnetic field inhomogeneities. This dependence on the field inhomogeneities can sometimes lead to unwanted signal loss and, therefore, constitutes an issue that needs to be addressed in the context of the quantification of the signal. In this paper, we demonstrate that this signal loss is associated with differences in phase evolution for the different coherence pathways that contribute to the triple quantum signal. When the TQ signal is acquired as a simple summation over coherence pathways, destructive interference between the individual coherences might ensue leading to signal loss in the images. We further demonstrate that by using a modified phase cycling scheme, the individual coherences can be obtained separately and then re-combined with the aid of a B_0 map to avoid the aforementioned signal loss. The effectiveness of this approach is demonstrated with NMR as well as imaging experiments.

2. Theory

As shown by Hancu et al. [4,5], for imaging applications the three-pulse triple quantum coherence transfer filter exhibits a more benign dependence on B_1 inhomogeneities than its four-pulse counterpart. This fact, together with the 40% decrease in the RF power, makes the three-pulse filter a more suitable choice for human studies.

This three-pulse coherence transfer filter is schematically depicted in the Fig. 1. It consists of a sequence of three pulses characterized by the same flip angle, θ, and phases φ_1, φ_2, φ_3. The delays τ_1 and τ_2 following the first and second pulses allow the creation of third-order coherences, and their propagation, respectively. Those coherences are converted into measurable, transversal magnetization by the last pulse. The presence of the B_0 inhomogeneities is described in terms of the parameter δ, defined as the deviation of the Larmor frequency, ω_0, from the frequency of applied RF, ω

$$\delta = \gamma B_0 - \omega. \tag{1}$$

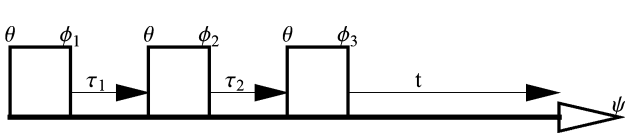

Fig. 1. The schematic representation of the three-pulse sequence.

Without loss of generality, we will assume for the remainder of this paper that the inhomogeneity parameter is constant across the sample volume (when this is not the case a B_0 map can be used to obtain the value of this parameter at every voxel on the imaged volume).

In a voxel characterized by a given value of the B_0 inhomogeneity parameter, δ, the recorded NMR signal at the time t, denoted $S_\delta(t)$, can be represented as a sum over coherence pathways, where the contribution of each coherence is a complex signal [6]. Because a pathway is completely characterized by the intermediate magnetic quantum numbers m_1, m_2, the total signal is given by a sum of 21 complex signals, with time-dependent amplitudes $A_{mn}(t)$ and time independent phases Ψ_{mn} [6]

$$S_\delta(t) = \sum_{m_1=-1}^{1} \sum_{m_2=-3}^{3} \exp(-\mathrm{i}\Psi_{m_1m_2}) A_{m_1m_2} \mathrm{e}^{-\mathrm{i}\delta t}. \tag{2}$$

Apart of their dependence on the acquisition time, the amplitudes A_{mn}, are functions of the flip angles and time delays, while the phases Ψ_{mn} are functions of time delays, pulses phases, receiver phase, and main magnetic field inhomogeneity

$$\begin{aligned} A_{mn} &\equiv A_{mn}(t;\tau_1,\tau_2,\theta), \\ \Psi_{mn} &\equiv \Psi_{mn}(\tau_1,\tau_2,\varphi_1,\varphi_2,\varphi_3,\psi,\delta). \end{aligned} \tag{3}$$

In the case of three identical RF pulses (i.e., same RF width and amplitude, but different phases), the four relevant amplitudes contributing to the triple quantum signal are given below (up to a normalization factor)

$$\begin{pmatrix} A_{-1,-3}(t) \\ A_{-1,3}(t) \\ A_{1,-3}(t) \\ A_{1,3}(t) \end{pmatrix} = u^1_{31}(\tau_1) u^3_{33}(\tau_2) u^1_{31}(t) \sin^5\theta \begin{pmatrix} -\cos^2(\theta/2)\sin^2(\theta/2) \\ -\cos^2(\theta/2)\sin^2(\theta/2) \\ \cos^4(\theta/2) \\ \sin^4(\theta/2) \end{pmatrix}. \tag{4}$$

For ions experiencing a biexponential relaxation behavior, in which the short and long T_2 relaxation times are T_S respectively T_L, the relaxation functions $u^k_{mn}(t)$ are given by

$$u^1_{31}(t) = (\mathrm{e}^{-t/T_S} - \mathrm{e}^{-t/T_L}) \text{ and } u^3_{33}(t) = \mathrm{e}^{-t/T_L}. \tag{5}$$

The phases associated with a given coherence pathway can be further decomposed as the sum of two terms,

$$\begin{aligned} &\Psi_{m_1m_2}(\tau_1,\tau_2,\varphi_1,\varphi_2,\varphi_3,\psi,\delta) \\ &\quad = \Phi_{m_1m_2}(\varphi_1,\varphi_2,\varphi_3,\psi) + \Delta_{m_1m_2}(\tau_1,\tau_2,\delta). \end{aligned} \tag{6}$$

The first term, Φ_{mn}, is defined by the receiver phase ψ and the pulse phases φ_i,

$$\Phi_{m_1m_2}(\varphi_1,\varphi_2,\varphi_3,\psi) = -\psi + (m_1\varphi_1 + (m_2 - m_1)\varphi_2 + (1 - m_2)\varphi_3), \tag{7}$$

while the second term describes the phase accumulation during the off-resonance propagation along the given coherence pathway, and is defined by the off-resonance parameter δ,

$$\Delta_{m_1m_2}(\tau_1,\tau_2,\delta) = (m_1\tau_1 + m_2\tau_2)\delta. \tag{8}$$

It should be noted that in the case of long RF pulses (as often is the case in MRI), the dephasing during the application of the RF could not be neglected. In this situation, the propagation times have to be modified according to the rules

$$\begin{aligned}\tau_1 &\to \tau_1 + T_{\text{eff}}\\ \tau_2 &\to \tau_2 + T_{\text{eff}},\end{aligned} \tag{9}$$

where T_{eff} is the effective length of the RF pulse, given in terms of the pulse length, T, and the flip angle, θ

$$T_{\text{eff}} = \frac{T}{\theta}\tan\left(\frac{\theta}{2}\right). \tag{10}$$

The proof of this relation, together with its limits of applicability is offered in Appendix B. Making use of this substitution, the propagation times are understood as the corrected expressions from Eq. (9), whenever they multiply the inhomogeneity parameter.

The phase cycling [4] is performed by adding the signals from N repetitions with different RF and receiver phases. The resulting signal, when acquired on-the-fly (i.e., automatically accumulated over each phase cycle by the scanner), can be written at any acquisition moment of time t as the sum

$$S_\delta^{\text{TQ}}(t) = \sum_{\varphi_1,\varphi_2,\varphi_3,\psi} S_\delta(t), \tag{11}$$

where the summation is performed over all combinations of RF phases φ_i and receiver phases ψ. By changing the order of summation in the last equation, an expression similar to Eq. (2) can be obtained, namely

$$S_\delta^{\text{TQ}}(t) = \sum_{m_1=-1}^{1}\sum_{m_2=-3}^{3} \mathrm{e}^{-\mathrm{i}\delta t} A_{m_1m_2}(t)\mathrm{e}^{-\mathrm{i}\Delta_{m_1m_2}} f_{m_1m_2}. \tag{12}$$

In this last expression, the extra-coefficients f_{mn} are sums over the RF phases

$$f_{m_1m_2} = \sum_{\varphi_1,\varphi_2,\varphi_3,\psi} \mathrm{e}^{-\mathrm{i}\Phi_{m_1m_2}}. \tag{13}$$

If the sign of the amplitudes $A_{mn}(t)$ are time independent, a phase cycling scheme can be designed such that

$$f_{m_1m_2} = \begin{cases} 0 & \text{if } |m_2| \neq 3 \text{ or } m_1 = 0,\\ N\,\text{sign}(A_{m_1m_2}) & \text{if } |m_2| = 3 \text{ and } m_1 \neq 0,\end{cases} \tag{14}$$

which brings the filtered signal in the form

$$S_\delta^{\text{TQ}}(t) = N \sum_{m_1=\pm1, m_2=\pm3} |A_{m_1m_2}(t)|\mathrm{e}^{-\mathrm{i}\delta t}\mathrm{e}^{-\mathrm{i}\Delta_{m_1m_2}}, \tag{15}$$

effectively filtering out the contributions from unwanted coherence pathways. The requirement of a time independent sign of amplitudes is satisfied for the system considered here, i.e., ions in isotropic slow fluctuating environment, as it can be easily seen from Eq. (5).

Such a phase cycling design is attractive since it has the property of producing the maximum on-resonance (i.e., when $\delta = 0$) signal

$$S_{\delta=0}^{\text{TQ}}(t) = |A_{1-3}(t)| + |A_{13}(t)| + |A_{-1-3}(t)| + |A_{-13}(t)|. \tag{16}$$

One particular implementation of this approach is the six-phase scheme used frequently in the literature [4]. This scheme corresponds to the following choices for the receiver (ψ) and RF (φ_i) phases

$$\begin{aligned}&\varphi_1 = \alpha_1 + \frac{\pi}{3}k, \quad \varphi_2 = \alpha_2 + \frac{\pi}{3}k, \quad \varphi_3 = 0,\\ &\psi = k\pi, \quad k = 0,\ldots,5.\end{aligned} \tag{17}$$

Using the filtering from Eq. (17), the corresponding coefficients f evaluate to expressions depending only on the starting phases of the cycle (α_1,α_2),

$$f_{m_1m_2}(\alpha_1,\alpha_2) = \begin{cases} 6\mathrm{e}^{-\mathrm{i}(m_1\alpha_1 + (m_2-m_1)\alpha_2)} & \text{if } |m_1| = 1, |m_2| = 3,\\ 0 & \text{otherwise.}\end{cases} \tag{18}$$

Finally, by choosing $\alpha_1 = \frac{\pi}{6}$, $\alpha_2 = \frac{2\pi}{3}$, the scheme fulfills the requirements of Eq. (14).

It has to be noted that this filtering scheme allows a residual signal, due to longitudinal recovery magnetization during the delay τ_1, to pass through the filter. In most imaging applications, the residual component is negligible because τ_1 is small compared with the longitudinal relaxation time T_1. Whenever this signal cannot be ignored (for example, in those 2D NMR experiments in which variable delays are used), the supplementation of the cycle with another six phases

$$\begin{aligned}&\varphi_1 = \alpha_1 + \pi + \frac{\pi}{3}k, \quad \varphi_2 = \alpha_2 + \frac{\pi}{3}k, \quad \varphi_3 = 0,\\ &\psi = \pi + k\pi, \quad k = 0,\ldots,5,\end{aligned} \tag{19}$$

cancels the T_1 contributions. For the sake of simplicity, we will assume these contributions negligible for the reminder of this paper (i.e., it is assumed that τ_1 is much smaller than T_1).

In the off-resonance case, the presence of Δ_{mn} phases in Eq. (15) leads to destructive interference between components associated with different coherence pathways. By combining the equations Eqs. (18) and (12) an analytic result is obtained for an arbitrary flip angles and inhomogeneity parameter

$$\begin{aligned} S^{\mathrm{TQ}}(\theta,\delta,\tau_1,\tau_2,t) &= \mathrm{e}^{-\mathrm{i}\delta t} S^{\mathrm{TQ}}_{\mathrm{ideal}}(\tau_1,\tau_2;t) F(\tau_1,\tau_2;\theta,\delta), \\ S^{\mathrm{TQ}}_{\mathrm{ideal}}(\tau_1,\tau_2,t) &= u^1_{31}(\tau_1) u^3_{33}(\tau_2) u^1_{31}(t), \\ F(\tau_1,\tau_2,\theta,\delta) &= \sin^5\theta \times \{\cos\delta\tau_1 \cos 3\delta\tau_2 \\ &\quad - \cos\theta \sin\delta\tau_1 \sin 3\delta\tau_2 \\ &\quad - \mathrm{i}\cos\theta(\cos\delta\tau_1 \sin 3\delta\tau_2 \\ &\quad + \cos\theta \sin\delta\tau_1 \cos 3\delta\tau_2)\}. \end{aligned} \tag{20}$$

From this expression, it is apparent that a reduction of the TQ signal from its maximum value to zero occurs for the offset parameter in the range $|\delta| \approx \pi/(2\tau_1)$ (in MRI applications τ_2 is much smaller than τ_1). For typical in vivo applications, the delay τ_1 is set to values maximizing the $u^1_{31}(\tau_1)$ functions, which usually leads to values around 5.0 ms. Therefore, variations in B_0 of the order of 50 Hz could destroy the TQ signal. Unfortunately, those variations are common during MRI in vivo applications, due to variations in tissue susceptibility that lead to B_0 inhomogeneities, which are difficult to compensate through shim optimization in a reliable and timely fashion.

A simple approach to correct for the signal variations described by Eq. (20) would be to experimentally determine θ and δ (which for MRI applications imply the acquisition of a B_1 map and a B_0 map) and use their values to compute the ideal signal. When the signal measurements are corrupted by noise (denoted η), Eq. (20) reads

$$S^{\mathrm{TQ}}(\theta,\delta,\tau_1,\tau_2,t) = \mathrm{e}^{-\mathrm{i}\delta t} S^{\mathrm{TQ}}_{\mathrm{ideal}}(\tau_1,\tau_2;t) F(\tau_1,\tau_2;\theta,\delta) + \eta(t), \tag{21}$$

and the corrected signal, $S^{\mathrm{TQ}}_{\mathrm{estimate}}$ would take the two term form

$$S^{\mathrm{TQ}}_{\mathrm{estimate}}(\delta,\tau_1,\tau_2;t) = \mathrm{e}^{-\mathrm{i}\delta t} S^{\mathrm{TQ}}_{\mathrm{ideal}}(\theta,\delta,\tau_1,\tau_2,t) + \frac{1}{F(\tau_1,\tau_2;\theta,\delta)}\eta(t). \tag{22}$$

Because the correction factor is less than one, $|F(\tau_1,\tau_2;\theta,\delta)| \leqslant 1$, this signal correction approach is not desirable since it decreases the signal-to-noise ratio (SNR) and also, in extreme cases when total signal cancellation occurs, F signal vanishes and no correction can be performed.

The effects of signal cancellation can be better compensated for by noting that the vanishing of the TQ signal under conditions of non-zero δ is not related to the intrinsic physics of the problem, but rather to the use of an inappropriate approach for the measurement of the TQ coherences. In other words, rather than correcting the effects at a data processing stage, a better approach would be to acquire the TQ signal under conditions that avoid the destructive interference between the coherence pathways. This new approach is presented in the text below.

From Eqs. (2) and (6), it is clear that, once the off-resonance parameter is fixed, for any choice of the RF and receiver phases, the measured signal is a linear combination of twelve complex quantities, $B_{m_1m_2}(t) = \exp(-\mathrm{i}\Delta_{m_1m_2})A_{m_1m_2}\mathrm{e}^{-\mathrm{i}\delta t}$, with time independent coefficients, i.e.,

$$S_\delta(t) = \sum_{m_1=-1}^{1}\sum_{m_2=-3}^{3} \exp(-\mathrm{i}\Phi_{m_1m_2}) B_{m_1m_2}(t). \tag{23}$$

If several measurements are performed using different settings for the receiver and RF phases, and these signals are stored independently (i.e., not added in real time by the scanner), Eq. (23) generates a linear system in the unknowns B_{mn}. By solving this linear system, the ideal TQ signal, as defined by Eq. (16), can then be obtained using the expression

$$S^{\mathrm{TQ}} \equiv \mathrm{e}^{\mathrm{i}\delta t}(\mathrm{e}^{\mathrm{i}\Delta_{-1,-3}}B_{-1,-3} + \mathrm{e}^{\mathrm{i}\Delta_{1,-3}}B_{1,-3} + \mathrm{e}^{\mathrm{i}\Delta_{-1,3}}B_{-1,3} + \mathrm{e}^{\mathrm{i}\Delta_{1,3}}B_{1,3}). \tag{24}$$

Because the number of unknown complex quantities in Eq. (23) is 12, 24 different acquisitions have to be performed to for determining all of the complex amplitudes B_{nm}. Under these conditions, use of an optimal acquisition scheme involves the proper choice of 24 sets of phases $(\varphi_1,\varphi_2,\varphi_3,\psi)$ such that the associated linear system can be solved for the complex amplitudes B_{mn}.

One possible choice of phase cycling that allows the solution of the system mentioned above would be to repeat the phase cycles from Eq. (17) four times, each time with different starting phases (α^j_1,α^j_2), $j = 1,2,3,4$. By using this acquisition, four signals S_j are obtained that are linear combinations of TQ components only

$$S_j(t) = \sum_{m_1=-1,1}\sum_{m_1=-3,3} f_{m_1m_2}(\alpha^j_1,\alpha^j_2) B_{m_1m_2}(t), \quad j = 1,2,3,4. \tag{25}$$

This reduces the dimensionality of the problem from 24 to 4 while also reducing the number of phases from 96 to 8. The starting phases chosen in this paper, together with the corresponding collected signals are displayed in Eq. (26)

$$\begin{cases} (\alpha^1_1,\alpha^1_2) = (30^\circ, 120^\circ) \\ (\alpha^2_1,\alpha^2_2) = (0^\circ, 0^\circ) \\ (\alpha^3_1,\alpha^3_2) = (60^\circ, 75^\circ) \\ (\alpha^4_1,\alpha^4_2) = (45^\circ, 90^\circ) \end{cases} \Rightarrow \begin{pmatrix} S_1 \\ S_2 \\ S_3 \\ S_4 \end{pmatrix} = 6 \begin{pmatrix} 1 & 1 & 1 & 1 \\ -1 & 1 & -1 & 1 \\ \mathrm{i} & -\mathrm{i} & \mathrm{i} & -\mathrm{i} \\ \frac{(1+\mathrm{i})}{\sqrt{2}} & \frac{(1-\mathrm{i})}{\sqrt{2}} & \frac{(-1+\mathrm{i})}{\sqrt{2}} & \frac{-(1+\mathrm{i})}{\sqrt{2}} \end{pmatrix} \begin{pmatrix} B_{-1,-3} \\ B_{-1,+3} \\ B_{+1,-3} \\ B_{+1,+3} \end{pmatrix}. \tag{26}$$

By solving the above system, the modified individual amplitudes B_{mn} are retrieved in the form of simple linear combinations of the measured signals,

$$\begin{pmatrix} B_{-1,-3} \\ B_{-1,+3} \\ B_{+1,-3} \\ B_{+1,+3} \end{pmatrix} = \frac{1}{8}\begin{pmatrix} 1-\mathrm{i} & 3+\mathrm{i} & 2(1+\mathrm{i}) & \sqrt{2}(1-\mathrm{i}) \\ -1 & 1 & -1 & 1 \\ \mathrm{i} & -\mathrm{i} & \mathrm{i} & -\mathrm{i} \\ \sqrt{2}(1-\mathrm{i}) & \sqrt{2}(1-\mathrm{i}) & \sqrt{2}(1-\mathrm{i}) & \sqrt{2}(1-\mathrm{i}) \end{pmatrix} \times \begin{pmatrix} S_1 \\ S_2 \\ S_3 \\ S_4 \end{pmatrix}. \tag{27}$$

From this system, the corrected TQ signal is then obtained using

$$S^{\mathrm{TQ}} \equiv \mathrm{e}^{\mathrm{i}\delta t}(\mathrm{e}^{\mathrm{i}\Delta_{-1,-3}}B_{-1,-3} + \mathrm{e}^{\mathrm{i}\Delta_{1,-3}}B_{1,-3} + \mathrm{e}^{\mathrm{i}\Delta_{-1,3}}B_{-1,3} + \mathrm{e}^{\mathrm{i}\Delta_{1,3}}B_{1,3}), \tag{28}$$

where the quantities Δ_{mn} contain the information about the off-resonance parameter. This is the approach proposed in this paper. Note that for imaging experiments, the method above is easily generalized through the use of spatial maps for the field inhomogeneity (i.e., by constructing the solution of the linear system above in a pixel-by-pixel fashion). The effectiveness of this approach is experimentally demonstrated in the sections below.

3. Experimental results

3.1. Phantom NMR experiments

All phantom NMR experiments were performed on a vertical bore, 7Tesla Bruker DMX300 spectrometer (Bruker AG, Germany). The samples consisted of agar gels containing sodium, as it is known that for sodium ions in such gels, third-order coherences form during relaxation [7]. For NMR experiments, a thorough shimming procedure was followed. To obtain a strong deuterium lock signal, the gel was prepared using D_2O instead of water. All chemicals used (10 cm^3 D_2O, 0.2 g NaCl, and 2 g agar powder) were acquired from Sigma–Aldrich (St. Louis, MO). The samples were prepared by bringing the mixture close to the boiling point while continuously mixing the NaCl and agar using a magnetic stirring plate and an uncovered Erlenmeyer flask. After mixing-in and dissolving the chemicals, the mixture was allowed to cool before being placed in 10 mm NMR tubes.

The NMR experiments presented here are aimed at emulating the signal originating from a single voxel in a MRI experiment. Because the off-resonance is one of the main experimental parameters, in order for those experiments to be meaningful, a high homogeneity of the B_0 field is required (the B_1 homogeneity is a less stringent requirement). In the light of those considerations, the sample was chosen as cylindrical in shape with a 10 mm diameter and a height of 4 cm (longer than the RF coil). For the purposes of shimming and calibration of the 90° pulse, one-pulse experiments (consisting of a RF pulse, 128 μs delay and acquisition with a sampling rate $d_w = 8$ μs) were used.

Shimming, a necessary step to mimic the single voxel signal, was performed in two stages. First, the deuterium lock signal was maximized by modifying the shim gradients. Second, a semi-automated procedure was used to optimize the shim gradients further, namely, a modification of the utility 'paropt' (the original being part of XWIN-NMR software suite) was used to maximize the amplitude of the sodium spectral peak, directly. The sensitivity of this approach is better than the one based exclusively on the lock signal, albeit at the expense of a 2-h increase in the total experimental time.

The calibration of the 90° pulse was performed using a constant-amplitude RF pulse experiment in which the length of the 90° pulse was varied while an array of one-pulse spectra was collected. For this procedure the pulse length was incremented from zero to 64 μs and the 90° pulse was found to correspond to a pulse length of 15.7 μs. The homogeneity of B_1 field, as estimated from the shape of spectra array, was found to be satisfactory.

The triple quantum experiments are performed with the pulse sequence depicted in Fig. 1. Relevant data acquisition parameters are $\tau_1 = 5$ ms, $\tau_2 = 64$ μs and the number of FID's accumulated $N = 150$. The data are accumulated at a rate $d_w = 16$ μs, with an original delay $d_e = 32$ μs. The $\tau_1 = 5$.ms value is close to the optimal value for the sample used; the maximum TQ signal should be obtained for the setting

$$\tau_{\mathrm{optim}} = \frac{T_{\mathrm{L}}T_{\mathrm{S}}}{T_{\mathrm{L}} - T_{\mathrm{S}}}\log\frac{T_{\mathrm{L}}}{T_{\mathrm{S}}}. \tag{29}$$

In Fig. 2, the plot marked (A) presents the measured conventional TQ FID data (dots) and its biexponential non-linear fit (solid line) to the formula

$$s(t) = A(\mathrm{e}^{-t/T_{\mathrm{L}}} - \mathrm{e}^{-t/T_{\mathrm{S}}}) + B. \tag{30}$$

Prior to fitting, the FID was scaled to its maximum value and phase corrected to zero and first-order. This procedure rotates the entire signal onto the real channel thereby improving the SNR (only noise is left on the imaginary component, as seen in the plot (B) of Fig. 2). The baseline returned by the fit, $B = 0.003$, is much smaller than the amplitude A, $A = 1.6$, proving that the signal is a good approximation to an ideal TQ signal (i.e., negligible bias in the fit).

The effectiveness of the coherence pathway decomposition is demonstrated in plot (C) of Fig. 2. The four individual contributions, associated with the different coherence pathways (the phase cycles required for their

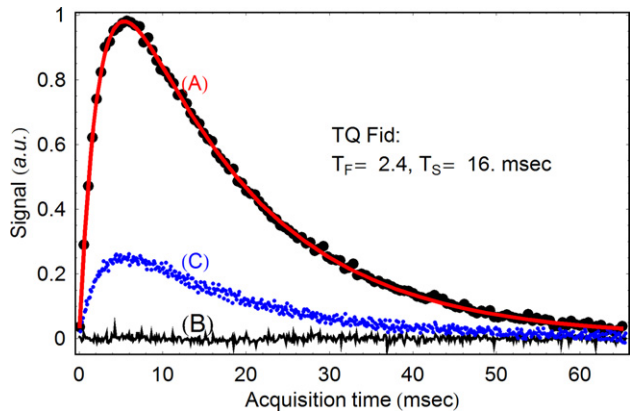

Fig. 2. The conventional TQ filtered FID. (A) The fit to a biexponential function (solid line) is presented together with the experimental real (dots) data points. (B) The imaginary (thin line) data points. (C) The four individual components (small dots) of the TQ signal are indistinguishable, proving the B_0 and B_1 homogeneity within the sample. The displayed data points are undersampled, to simplify the graph.

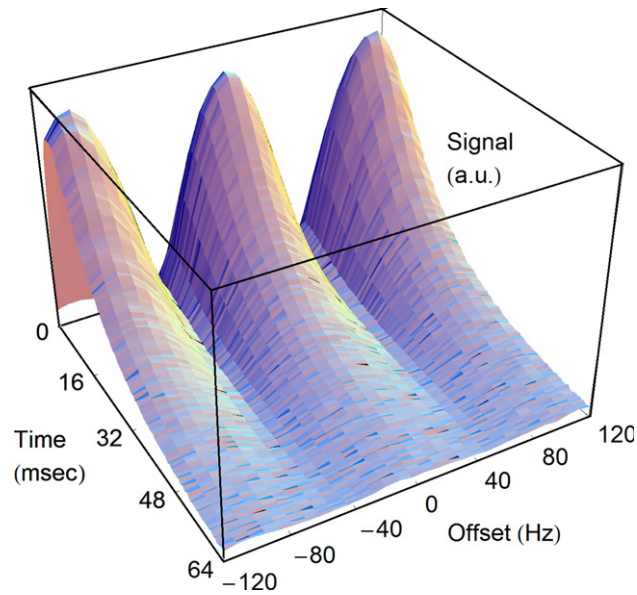

Fig. 3. The acquired classical TQ FID magnitudes are displayed as a function of acquisition time and the off-resonance parameter. The vanishing of the TQ signal is expected around $\delta = \pm 50$ Hz lines and it is well demonstrated by the plot.

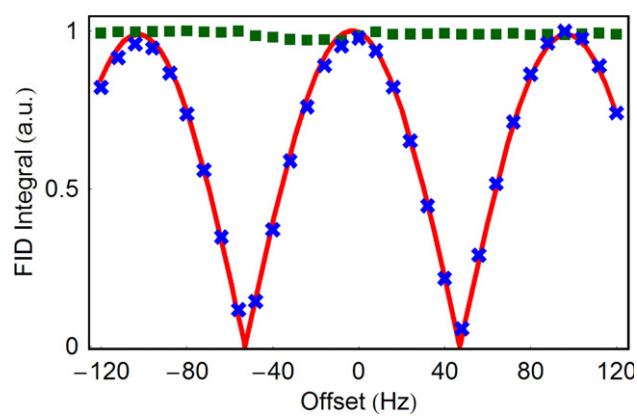

Fig. 4. Integral of the conventional TQ FID as a function of the off resonance parameter (crosses). The theoretical function (solid line) agrees well with experimental data. The modified TQ acquisition data (boxes) shows less variation with the off-resonance parameter.

acquisition are given in Appendix A) are displayed using small dots, and are practically undistinguishable from each other. The fact that all the components have the same amplitudes and shapes demonstrates good B_1 homogeneity and B_0 homogeneity. Their sum resembles the classical TQ signal (plot A, Fig. 2) within the experimental errors. Those facts are another justification for considering the signal in Fig. 2 as an adequate approximation a single voxel signal.

For an MRI experiment, the off-resonance parameter varies across the volume of interest. To verify the accuracy of the modified TQ acquisition scheme, four NMR experiments were performed in a 2D fashion, for each of the starting phases presented in Eq. (26). In each experiment, the RF frequency was incremented from −120 to 120 Hz in 8 Hz steps. For every frequency setting, the TQ FID was acquired using the same settings as in the 1D experiment. The number of FID's averaged was reduced from 150 to 60, to shorten the total experiment time. The dependence of conventional TQ signal (corresponding to the first choice of phases) as a function of the applied RF frequency is presented in Fig. 3. Since a rough surface is harder to visualize, the surface was smoothed with a running average algorithm.

The B_{mn} solution from Eq. (27) is then computed for each frequency offset, followed by the demodulations and summations described by Eq. (28). At every frequency point, the calculated solutions reproduce well the classical on resonance TQ signal. To compare the efficiencies of the modified and classical schemes, in a quantitatively manner, the integrals of the acquired TQ signals are presented in Fig. 4, as a function of frequency. The crosses correspond to the conventional acquisition scheme. As expected, they follow the dependency ($\cos\delta\tau_1 \cos\delta\tau_2$), which is displayed as a solid line in the plot. The boxes correspond to the modified acquisition scheme. Clearly, the more benign variation of the TQ signal intensity as a function of the off-resonance parameter in this modified acquisition scheme makes it suitable for imaging applications.

3.2. MRI phantom experiments

The MR imaging experiments were performed on a whole-body, 3 T, MRI scanner (GEHT) using a custom-built sodium RF coil and a twisted projection imaging (TPI) sequence [8] (214 views). The repetition time was set to 120 ms, leading to a total experimental time of 26 s when one RF excitation is performed for each

view. A cylindrical shaped (length $L = 12$ cm, diameter $\varnothing = 12$ cm), homogenous phantom filled with 10% agar gel, was used.

Two single quantum (SQ) data sets were obtained by exciting the sample with hard pulses (pulse width $p_w = 400$ μs, $T_{\text{eff}} \sim 255$ μs) and using echo times (the delay from the end of the pulse to the beginning of acquisition period) $T_{\text{E1}} = 10$ and $T_{\text{E2}} = 11.5$ ms. The reconstructed images, obtained by using a regridding algorithm, are $64 \times 64 \times 64$ complex matrices of complex values. Using the two SQ images, the off-resonance parameter δ, for each voxel, was obtained from the phases of SQ images, to generate a phase map

$$\delta = \frac{\phi_2 - \phi_1}{T_{\text{E2}} - T_{\text{E1}}} \tag{31}$$

with ϕ_1, ϕ_2 being the phases, in that voxel, of the reconstructed images corresponding to the echo times T_{E1} and T_{E2}, respectively. Phase unwrapping was not necessary, as the phase variation from one pixel to another were typically small. To speed up the analysis, an image mask (with a threshold set at 30% of the maximum SQ image intensity) was generated from the SQ image so that the solution of the linear system described above was not performed in areas of zero signals.

Triple quantum (TQ) images are acquired with a modification of TPI sequence, as presented in [4]. The separations between pulses were $\tau_1 = 7.0$ and $\tau_2 = 0.5$ ms. The echo time is $T_{\text{E}} = 10.0$ ms. Those values correspond to the highest TQ signal for the phantom used. Four different experiments, corresponding to the four phase cycles from Eq. (26), were performed, the duration of each TQ experiment being six times longer than the SQ (there were six excitations per view in this phase cycling scheme), i.e., 2 min 34 s. Image reconstruction was performed using the same algorithm, with the same parameter settings as used for the SQ images.

Figs. 5A and B present the middle slices from the phase map and the SQ magnitude, respectively. The presence of large inhomogeneities in the middle of the phantom is clearly illustrated in the phase map. This B_0 map has the expected shape for a finite cylinder, placed in a uniform magnetic field.

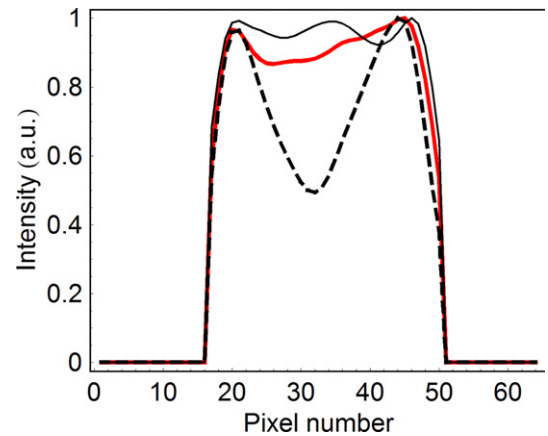

Fig. 6. The conventional TQ profile (dashing) and modified TQ (thick solid line), together with the SQ profile (thin solid line). The variation in the reconstructed intensity observed in the corrected TQ image is due to the presence of B_1 inhomogeneity, ringing and intravoxel dephasing. However, a significant source of variation has been removed by using the modified TQ scheme.

In Fig. 5C the conventional TQ image is presented. As expected from the phase map, the TQ signal is diminished in the center of the phantom.

The Fig. 5D, which is the image obtained from modified TQ acquisition, illustrates the removal of the artifacts due to the B_0 inhomogeneities. Finally, in Fig. 6 a 1D illustration of the differences between the conventional and modified TQ results is given. The data were sampled along the dotted lines presented in each picture.

4. Discussion

Quantitative sodium MRI requires the removal of image artifacts due to B_0 inhomogenities. These field inhomogeneities, which arise primarily due to variations in tissue susceptibility, lead to different effects in MRI.

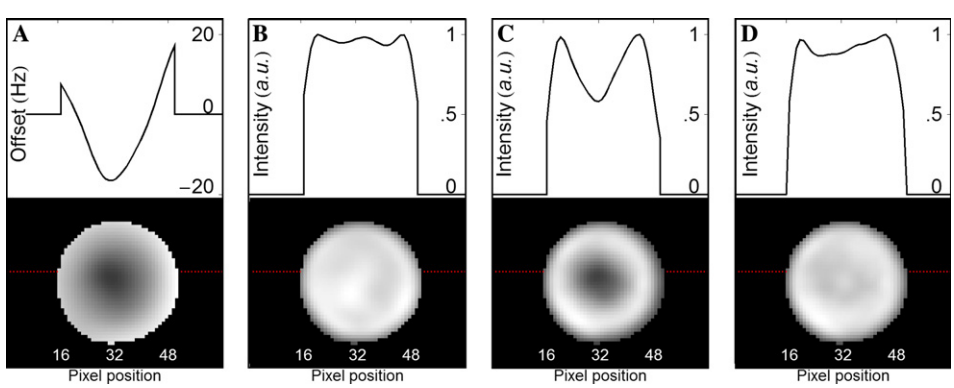

Fig. 5. Selected partitions from the experimentally acquired 3D images of a cylindrical phantom. The dotted line illustrates the direction along which 1D profiles (upper part of the plots) were drawn. (A) B_0 map (B) SQ magnitude (C) Classical TQ acquired image exhibiting the low intensity region (D) The TQ image acquired with the modified sequence, the low intensity region in the center of image is largely removed.

T_2^* effects [9–11], and the distortion of k-space trajectories [12] are the major difficulties encountered in conventional proton MRI. A different manifestation of B_0 inhomogeneities artifacts that leads to signal loss in MQF MRI has been analyzed in this paper. The signal loss arises because of the way that various coherence pathways add up to create the measured signal; namely, the B_0 inhomogeneity introduces phase differences between such coherence pathways, leading to signal cancellation. This phenomenon is akin to intra-voxel dephasing in conventional gradient echo techniques, except for the fact that it does not have an explicit voxel size dependence (i.e., it is also present in the limit in which the voxel size is infinitely small).

This phenomenon was demonstrated here for sodium TQ experiments, but it can also manifest in other MQF experiments provided that the following conditions are met: the MQF signal has contributions from multiple coherence pathways, non-identical dephasing occurs along different pathways, and the on-resonance conditions is not fulfilled.

One solution to this signal loss would be to design the filtering scheme in such a way that only one coherence path passes through the filter. This approach, however, would necessarily lead to lower SNR. In an attempt to preserve the SNR of the experiment, while avoiding the aforementioned cancellation, a different acquisition scheme is introduced. The main concept behind this approach is that concurrent acquisition of all coherence pathways can be performed so long as an appropriate encoding mechanism allows their separation in post-processing.

This concept was implemented in this paper through the use of four different TQ filtered acquisitions, which could in principle require extending the imaging time. However, as the relative contribution of each of these TQ acquisitions can be predicted with the aid of a B_0 map, it is possible to prospectively design the phase cycling scheme so that the increase in imaging time can be minimized. This approach, although not explicitly shown in this paper, is well-supported by the experimental data shown above and it would be developed in a future work.

Our MRI results illustrate the significance of the destructive interference between coherence pathways when the field inhomogeneity is not non-negligible. The correction approach shown here was also found to be effective at mitigating the ensuing signal loss and it is one of many improvements that could be made to maximize the SNR. Further extensions to this approach are, in fact, possible. For example, including a B_1 correction prior to the solution of the linear system presented above might improve the recovery of the MQF signal. Finally, another aspect that could be improved upon is the removal of signal loss during RF excitation, i.e., by correcting the Δ_{mn} factors, signal dephasing during the RF pulses can be minimized.

5. Conclusions

A description of the effects of B_0 inhomogeneities on TQ filtered sodium MRI using a three-pulse coherence transfer filter has been presented. We have demonstrated that in the presence of large B_0 inhomogeneities significant signal loss arises due to destructive interference between the different coherence pathways. We have also shown that this effect can be eliminated through the separate acquisition of the TQ coherences followed by their addition after B_0 correction with the aid of a B_0 map. Our results demonstrate that this approach is well suited for TQ sodium MRI experiments using clinical MRI scanners.

Acknowledgments

C.T. thanks Ileana Hancu for stimulating discussions on sodium NMR and MRI experiments. This work was supported in part by PHS Grants 1R21CA87805, 1R01NS44818, and 1R01EB000291.

Appendix A. Selection of individual components

The selection of individual components, i.e., corresponding to each of the pathways contributing to TQ signals, is accomplished by using cycling schemes with 10 phases

$$\phi_1 = \alpha_1 k\pi/5, \quad \phi_2 = \alpha_2 k\pi/5, \quad \phi_3 = \alpha_3 k\pi/5, \quad \psi = k\pi \quad k = 0, \ldots, 9 \tag{A.1}$$

with the coefficients for each component given in the following table

(m_1, m_2)	α_1	α_2	α_3
$(-1, -3)$	1	0	-2
$(-1, +3)$	1	2	1
$(+1, -3)$	1	0	1
$(+1, +3)$	1	4	7

These phase cycles have been introduced and discussed elsewhere [13].

Appendix B. Finite pulse width

Obviously, in the MRI case of long pulses, a significant dephasing occurs during the application of RF pulses. The main point in discussing the finite pulse width is to replace the form of Δ_{mn} quantities in Eq. (8) with expressions taking in account the propagation of coherences during the RF pulses

$$\Delta_{m_1 m_2} = (m_1(\tau_1 + T_{\text{eff}}) + m_2(\tau_2 + T_{\text{eff}}))\delta. \tag{B.1}$$

The origin of this substitution is briefly presented in this paragraph, as the theory behind those manipulations (the representations of rotation group and the reduced Wigner functions) is well known. In slightly different notations, in [14] it is shown that the off-resonance pulse is equivalent to an on-resonance pulse followed and preceded by rotations around the B_0 axis.

In our notations, the off-resonance pulse characterized by the RF frequency ω ($\delta = \omega_0 - \omega$), constant amplitude B_1 ($\omega_1 = \gamma B_1$), duration T and phase φ, is described as the finite rotation with the angle—$\tilde{\theta}$, around an axis characterized by the latitude—η and by the azimuth φ where

$$\theta = \omega_1 T, \quad \psi = \delta T, \quad \tilde{\theta} = \sqrt{\theta^2 + \psi^2}, \quad \tan\eta = -\psi/\theta. \tag{B.2}$$

The description in terms of Euler angles is preferred due to the simple form taken by the action of rotation operators, when expressed in terms of the Euler angles $(\alpha_L, \beta, \alpha_R)$. The relationship is given, whenever $\theta \in [0, \pi]$ and $\eta \in [-\pi/2, \pi/2]$, by the parametric expressions

$$\alpha_L = \alpha - \left(\varphi + \frac{\pi}{2}\right), \quad \alpha_R = \alpha + \left(\varphi + \frac{\pi}{2}\right),$$
$$\beta = 2\arcsin\left(\cos\eta \sin\frac{\theta}{2\cos\eta}\right), \tag{B.3}$$

where as shown in [14]

$$\alpha = \arctan\left(\sin\eta \tan\left(\frac{\theta}{2\cos\eta}\right)\right). \tag{B.4}$$

As a consequence, when acting on a linear space in which the angular momentum components are represented by the operators $(\mathbf{J}_X, \mathbf{J}_Y, \mathbf{J}_Z)$, the off-resonance pulse $\mathbf{P}(\theta, \varphi, \delta)$, is represented in terms of the on-resonance pulse $\mathbf{P}(\theta, \varphi)$ by the operator

$$\mathbf{P}(\theta, \varphi, \delta) = \exp(\mathrm{i}\delta T_{\theta,\delta}\mathbf{J}_Z)\mathbf{P}(\beta, \varphi)\exp(\mathrm{i}\delta T_{\theta,\delta}\mathbf{J}_Z), \tag{B.5}$$

where the effective length of the pulse is introduced, and it has the exact expression

$$T_{\theta,\delta} = \frac{\cos\eta}{\theta\sin\eta}\arctan\left(\sin\eta\tan\left(\frac{\theta}{2\cos\eta}\right)\right). \tag{B.6}$$

At this point we note that for flip angles around $\pi/2$ and small inhomogeneities, the following approximations could be used, $\cos\eta \cong 1$, $\sin\eta \cong \tan\eta \cong \eta = -\psi/\theta$, from where

$$\begin{cases} \beta = 2\arcsin\left(\cos\eta\sin\frac{\theta}{2\cos\eta}\right) \cong \theta, \\ T_{\theta,\delta} = \frac{T\cos\eta}{\theta\sin\eta}\arctan\left(\sin\eta\tan\left(\frac{\theta}{2\cos\eta}\right)\right) \cong \frac{T}{\theta}\tan\left(\frac{\theta}{2}\right) \equiv T_\theta. \end{cases} \tag{B.7}$$

Through numerical comparisons with the exact expressions, the approximations are can be shown to be accurate (error less than 1%) whenever $\theta \in [60°, 120°]$ and $\psi \in [-20°, 20°]$. Those conditions are easily satisfied for typical experiments; therefore, the off-resonance pulse is described in terms of the on-resonance pulse with the same flip angle, and an effective length T_θ depending on the flip angle, only. In terms of associated rotation, the approximation becomes

$$\mathbf{P}(\theta, \varphi, \delta) = \exp(\mathrm{i}\delta T_\theta \mathbf{J}_Z)\mathbf{P}(\theta, \varphi)\exp(\mathrm{i}\delta T_\theta \mathbf{J}_Z), \tag{B.8}$$

which can be interpreted as the fact that the off-resonance pulse is equivalent with the on-resonance pulse preceded and followed by T_θ free evolution periods. When this expression is used for the coherence transformation, the replacement rule given in Eq. (B.1) is obtained. In this paper, the flip angle is assumed to be close to the ideal 90° pulse, therefore $T_\theta \sim T(2/\pi)$.

References

[1] P.M. Winter, N. Bansal, Triple-quantum-filtered (23)Na NMR spectroscopy of subcutaneously implanted 9l gliosarcoma in the rat in the presence of TmDOTP(5-1), J. Magn. Reson. 152 (1) (2001) 70–78.

[2] V.D. Schepkin et al., Sodium TQF NMR and intracellular sodium in isolated crystalloid perfused rat heart, Magn. Reson. Med. 39 (4) (1998) 557–563.

[3] I. Hancu et al., In vivo triple-quantum-filtered sodium imaging of brain neoplasms in humans, in: Eight Scientific Meeting International Society for Magnetic Resonance in Medicine, Denver, Colorado, 2000.

[4] I. Hancu, F.E. Boada, G.X. Shen, Three-dimensional triple-quantum-filtered ^{23}Na imaging of in vivo human brain, Magn. Reson. Med. 42 (6) (1999) 1146–1154.

[5] R. Reddy et al., Multiple-quantum filters of spin-3/2 with pulses of arbitrary flip angle, J. Magn. Reson. B 104 (1994) 148–152.

[6] C. Tanase, F. Boada, Robust Measurement of spin 3/2 transverse relaxation in the presence of both B_0 and B_1 inhomogeneities, in: Experimental Nuclear Magnetic Resonance Conference, Asilomar, California, 2004.

[7] D. Woessner, N. Bansal, Temporal characteristics of NMR signals from spin 3/2 nuclei of incompletely disordered systems, J. Magn. Reson. 133 (1) (1998) 21–35.

[8] F. Boada et al., Fast three dimensional sodium imaging, Magn. Reson. Med. 37 (1997) 706–715.

[9] V. Stenger, F. Boada, D. Noll, Three-dimensional tailored RF pulses for the reduction of susceptibility artifacts in T_2^*-weighted functional MRI, Magn. Reson. Med. 44 (2000) 525–531.

[10] R. Constable, Functional MR imaging using gradient-echo echo-planar imaging in the presence of large static field inhomogeneities, J. Magn. Reson. Imaging 5 (6) (1995) 746–752.

[11] Q. Yang et al., Removal of local field gradient artifacts in T_2^*-weighted images at high fields by gradient echo slice excitation profile imaging, Magn. Reson. Med. 39 (1998) 402–409.

[12] D. Noll et al., Deblurring for non-2D Fourier transform magnetic resonance imaging, Magn. Reson. Med. 25 (2) (1992) 319–333.

[13] C. Tanase, F. Boada, Algebraic description of spin 3/2 dynamics in NMR experiments, J. Magn. Reson., (2005) doi:10.1016/j.jmr.2004.12.009.

[14] D.E. Freed, M.D. Hurlimann, U.M. Scheven, The equivalence between off-resonance and on-resonance pulse sequences and its application to steady-state free precession with diffusion in inhomogeneous fields, J. Magn. Reson. 162 (2) (2003) 328–335.